This draft was prepared using the LaTeX style file belonging to the Journal of Fluid Mechanics 1

Modulation of elasto-inertial transitions in Taylor-Couette flow by small particles

Tom Lacassagne[1,3]†, Theofilos Boulafentis [1] Neil Cagney[2], and Stavroula Balabani[1]‡

[1]FLUME, Department of Mechanical Engineering, University College London (UCL), London, WC1E 7JE, UK

[2]School of Engineering and Materials Science, Queen Mary University of London, UK

[3]IMT Nord Europe, Institut Mines-Télécom, Univ. Lille, Centre for Energy en Environment, F-59000 Lille, France

(Received xx; revised xx; accepted xx)

Particle suspensions in non-Newtonian liquid matrices are frequently encountered in nature and industrial applications. We here study the Taylor-Couette flow (TCF) of semi-dilute spherical particle suspensions (volume fraction $\leqslant 0.1$) in viscoelastic, constant viscosity liquids (Boger fluids). We describe the influence of particle load on various flow transitions encountered in TCF of such fluids, and on the nature of these transitions. Particle addition is found to delay the onset of first and second order transitions, thus stabilising laminar flows. It also renders them hysteretic suggesting an effect on the nature of bifurcations. The transition to elasto-inertial turbulence is shown to be delayed by the presence of particles, and the features of elasto-inertial turbulence (EIT) altered, with preserved spatio-temporal large scales. These results imply that particle loading and viscoelasticity, which are known to destabilize the flow when considered separately, can on the other hand compete with one-another and ultimately stabilize the flow when considered together.

Key words: Suspension, Elasto-inertial turbulence, Viscoelasticity, Taylor-Couette

1. Introduction and background

Particle suspensions in non-Newtonian liquids are frequently encountered in nature and industrial applications, such as cement, toothpaste, 3D printing material or drilling muds, (Ovarlez *et al.* 2015; Dagois-Bohy *et al.* 2015; Fang *et al.* 2017; Liu *et al.* 2015). Multiple non-linear effects, such as non-linear dynamic behaviour of the liquid phase, fluid-particle and particle-particle interactions, can co-exist in such systems giving rise to complex rheology and macroscale flow dynamics. Significant efforts have been made in recent years to derive constitutive equations to accurately describe the physical properties of these complex fluid systems (Morris 2020; Yang & Shaqfeh 2018*a*,*b*; Gillissen & Wilson 2019). However, experimental data is still needed to better understand the effects of such complex particle suspensions on the stability and transitions in macroscale flows, in order to link microscopic and macrosopic behaviour.

For that purpose, one can advantageously use the "hydrogen atom" of fluid mechanics

† Email address for correspondence: tom.lacassagne@imt-nord-europe.fr
‡ Email address for correspondence: s.balabani@ucl.ac.uk

(Fardin *et al.* 2014), Taylor-Couette flows (TCF): the flow developing between two concentric cylinders at least one of which is rotating. This simplified geometry is widely used in rheometry and also to investigate stability and transitions in various fluids, including for example non-Newtonian polymeric solutions (see e.g. Martínez-Arias & Peixinho (2017); Cagney *et al.* (2020); Dutcher & Muller (2013); Lacassagne *et al.* (2020, 2021) among many others), and particle suspensions in Newtonian solvents (Majji & Morris 2018; Majji *et al.* 2018; Ramesh *et al.* 2019; Ramesh & Alam 2020; Morris 2020; Gillissen & Wilson 2019; Gillissen *et al.* 2020). This last topic has recently benefited from a set of comprehensive experimental studies describing the effects of low particle concentrations on mixing in TCF (Rida *et al.* 2019; Dherbécourt *et al.* 2016), TCF dynamics of dense particle suspensions with sedimentation and re-suspension (Saint-Michel *et al.* 2017, 2019), and the effects of intermediate particle concentrations on high order flow transitions (Majji & Morris 2018; Majji *et al.* 2018; Ramesh *et al.* 2019; Ramesh & Alam 2020; Dash *et al.* 2020; Baroudi *et al.* 2020). As part of the latter, it has been shown that the presence of particles globally tends to destabilise the flow (Majji *et al.* 2018; Ramesh *et al.* 2019; Dash *et al.* 2020), as predicted by modelling approaches (Gillissen & Wilson 2019). It was also found to promote additional non-axisymetric flow states (Ramesh *et al.* 2019; Dash *et al.* 2020) and the co-existence of flow states (Majji *et al.* 2018; Ramesh & Alam 2020; Dash *et al.* 2020), thus altering the common Couette Flow (CF) - Taylor Vortex Flow (TVF) - Wavy Taylor Vortex flow (WTVF) transition encountered in TCF of Newtonian fluids with the inner cylinder only rotating.

When considering TCF of polymer solutions, it has been consistently shown that their non-Newtonian features also tend to destabilize the base and first order laminar flows (Cagney *et al.* 2020; Lacassagne *et al.* 2021), give rise to additional flow states (see e.g. Dutcher & Muller (2013); Lacassagne *et al.* (2020); Groisman & Steinberg (1996)), and transition to low Re turbulent-like states such as elastic (Groisman & Steinberg 2004) or elasto-inertial turbulence (Dutcher & Muller 2013; Lacassagne *et al.* 2020, 2021). However, it was recently highlighted experimentally that various non-Newtonian features of the same fluid may not combine towards destabilizing the flows, but rather compete, with shear-thinning mediating elasto-inertial transitions (Cagney *et al.* 2020; Lacassagne *et al.* 2021). Questions then arise when considering TCF of suspensions in non-Newtonian fluids. Are the two complex features of the fluid, namely elasticity and the presence of particles, expected to act in synergy to destabilise the flow? Will the presence of particles mediate elasto-inertial instabilities? To address these questions, we here study the TCF of semi-dilute mono-disperse spherical particle suspensions (polymethylmethacrylate particles, GoodFellow, United Kingdom, $0.01 \leqslant \phi \leqslant 0.1$, with ϕ the particle volume fraction) in a viscoelastic, fluid with constant shear-viscosity (Boger fluid made of polyacrylamide dissolved in a water glycerol mixture as in Lacassagne *et al.* (2020)), the density of which matched that of the particles ($\rho = 1198$ Kg.m^{-3})

2. Experimental details

The steady-shear rheology of suspensions was measured using an ARES rheometer (TA Instruments) equipped with a Couette geometry (1 mm gap). Characterisation was systematically performed on the Boger matrix itself and on the particle suspension in Boger fluid, before and after the Taylor-Couette experiments (the exact same sample as that used for the TCF experiment). This last step allowed us to verify that the samples did not experience polymer degradation during the experimental protocol. Additional characterisation of the water-glycerol mixture with and without particles were also performed separately. Examples of viscosity curves are reported in figures 1

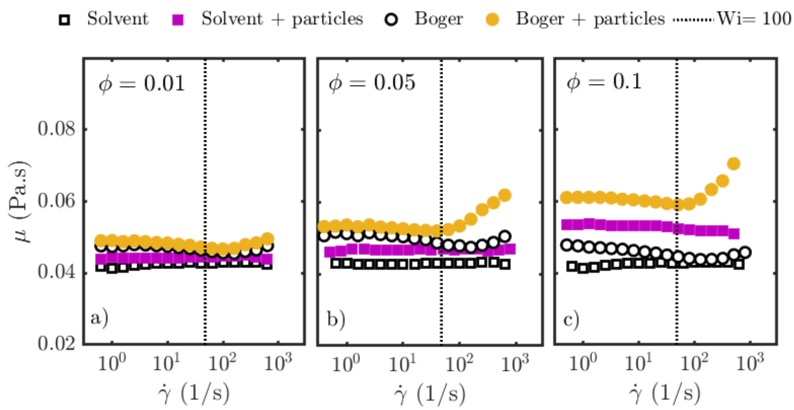

Figure 1: Steady shear viscosities, for particle-loaded solvent and particle-loaded Boger fluid, for all three values of ϕ, together with systematic characterisations of particle-free solvent and Boger matrix. Vertical dashed lines are plotted at Wi=100.

a to c. The suspensions in Boger fluids (full circles) exhibited constant viscosity for a wide range of shear-rates. An increase in viscosity was observed for shear rates above 100 s^{-1} which could not be ascribed to inertial instabilities (which generally do not occur when the inner cylinder is fixed, as was the case here), but rather to purely elastic instabilities. The dashed lines in figure 1 highlight that this apparent thickening only occurs when the Weissenberg number exceeds 100 ($Wi = t_e\dot{\gamma}$, where $\dot{\gamma}$ is the strain rate and t_e is the relaxation time), in agreement with the results of Schaefer *et al.* (2018) at similar curvatures. A similar behaviour was also observed for particle free Boger fluids (empty circles on all sub-plots in figure 1), and for additional measurements performed with a plate-plate geometry (not reported here, see also Groisman & Steinberg (2004)) confirming this hypothesis. The effective viscosity was then taken as the average viscosity value on the plateau region of the curve. Values for this average viscosity are reported in table 1, averaged on all tests at similar ϕ. Oscillatory-shear measurements performed with the same rheometer and geometry showed that the addition of particles did not modify the elastic and storage moduli G' and G" of the liquid. The apparent elastic time-scale of the Boger fluid, which was estimated from the crossover point between G' and viscosity corrected G" curves as detailed in Lacassagne *et al.* (2020), was thus not altered by the presence of particles and found equal to $t_e = 0.21$ s.

The Taylor-Couette flow cell is displayed in figure 2 and is similar to the one used in Cagney *et al.* (2020); Lacassagne *et al.* (2020, 2021) (the reader may refer to those works for further details). The axial length was H = 135 mm, and the inner and outer radii were r_i =21.66 mm and r_o =27.92 mm, respectively. This corresponds to a gap width of d = 6.26 mm, a radius ratio of $\eta = r_i/r_o = 0.776$, curvature ratio $\epsilon = d/r_i = 0.289$ and an aspect ratio $AR = H/d = 21.56$ (figure 2), which places the setup in the large gap and high curvature limits. The particle nominal diameter was d_p = 48 μm. The gap to particle diameter ratio was d/d_p = 131, well in the small particle limit. Three types of experiments were performed: ramp-up (RU, acceleration of the inner cylinder), ramp-down (RD, deceleration) and steady state experiments (STS, constant rotation speed of the inner cylinder recorded for a given time span). RU and RD tests allowed the flow transitions and instabilities to be characterised over a continuous range of cylinder rotation speed and the nature of the bifurcations to be discussed. STS tests allowed a

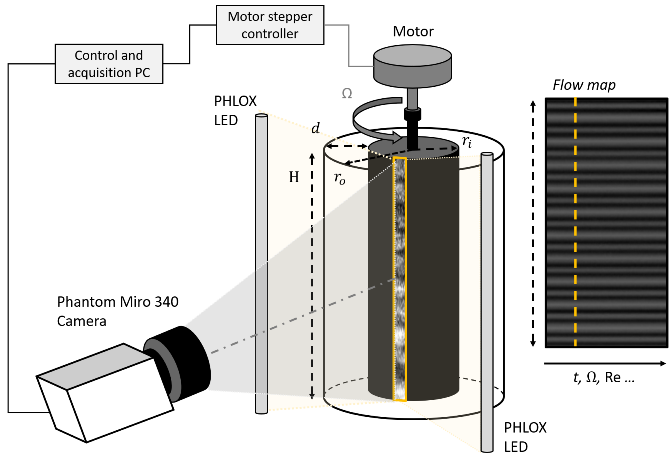

Figure 2: Schematic of the experimental set-up showing the Taylor-Couette cell, visualisation arrangement, and flow map construction.

specific flow state to be examined with greater temporal resolution. The rotation speed of the inner cylinder, Ω, and the co-responding Reynolds number defined as Re$=\rho\Omega r_i d/\mu$ were the main control parameters in the experiments. The particle Reynolds number, $\mathrm{Re}_p = \rho\Omega r_i d_p/\mu$, was $\mathrm{Re}_p \ll$Re and $\mathrm{Re}_p \sim \mathcal{O}(1)$ at maximum Ω. Two other non-dimensional groups can be used to decsribe the experiments: the Weissenberg number, defined with respect to the average strain rate across the fluid, $Wi = t_e\Omega r_i/d$, and the Elastic number El=Wi/Re which does not depend on Ω but solely on fluid properties. El ranged from 0.21 at $\phi = 0$ (see also Lacassagne *et al.* (2020)) to 0.28 at $\phi = 0.1$, due to the change in viscosity (see table 1). Acceleration or deceleration of the inner cylinder was performed in a quasi-steady fashion (with the non-dimensional rate $\Gamma_0 < 1$ as defined in table 1, see also Dutcher & Muller (2009); Lacassagne *et al.* (2021)). The flow structure was captured by adding a very small quantity (volume fraction of the order of 10^{-4}, with negligible effect on the flow (Gillissen *et al.* 2020)) of reflective flakes to the fluid (Pearl lustre pigments, L.Cornelissen & Son, United Kingdom) illuminating using a white light source (PHLOX, France) and imaging using a high speed camera (Phantom Miro 340, Vision Research, US) as detailed in previous works (Gillissen *et al.* 2020; Cagney *et al.* 2020; Lacassagne *et al.* 2021) (see figure 2).

The acquisition frequency was chosen, such that it was sufficiently high to capture all frequencies of the flow while allowing the experiment to be recorded in a single run, considering the limitations of camera memory. The recording frequencies and experimental parameters used with each working fluids for RU and RD experiments are summarized in table 1. STS experiments were recorded at a higher frequency than RU and RD experiments, 1000 fps. Flow maps and frequency maps were constructed with the protocol described in Lacassagne *et al.* (2021).

3. Results and discussion

3.1. *Overview and transitions*

The data presented in this section relates only to Boger fluids with particle loading. A sample transition sequence for $\phi = 0.1$ is presented in figure 3, where a) is the flow

ϕ	μ (Pa s)	N_{RU}	N_{RD}	Γ_0	f_{acq} (fps)
0	0.0475	6	6	0.30	90
0.01	0.0494	6	5	0.35	200
0.05	0.0565	4	4	0.35	200
0.10	0.0627	7	4	0.31	180 or 250

Table 1: Summary of experimental parameter for ramp-up (RU) and ramp-down (RD) experiments. N_{RU} and N_{RD} correspond to the number of repeated experiments for RU and RD, respectively. $\Gamma_0 = \frac{\mathrm{dRe}}{\mathrm{d}t^*} = \frac{\rho^2 r_i d^3}{\mu^2}\frac{\mathrm{d}\Omega}{\mathrm{d}t}$ is the non-dimension acceleration rate, with $t^* = t/t_v$ the time scaled by the viscous time-scale $t_v = \rho d^2/\mu$.

map (Re-space diagram) for $\phi = 0.1$ during a RU experiment, b) is the corresponding frequency map, and c) and d) are flow maps from STS experiments performed at Re=133 and Re=200, respectively. e) shows frequency spectra extracted from b) and corresponding to flow states described in c) and d). Finally, f) and g) display flow and frequency maps corresponding to a) and b) but for a RD experiment. A visual difference in flow transitions between RU and RD can be noted, and will be discussed later.

In CF the time-space diagrams (a,f) are homogeneous, with all flakes oriented in the azimuthal direction. When TVF arises, the flakes orientation in relation to Taylor Vortices gives rise to a banded structure. CF (or TVF) are steady in time and not associated with any characteristic frequencies on the frequency map (figure 3 b,g), other than the inner cylinder rotation frequency, that is captured by the method. The end of CF is identified from the flow maps when spatial structures appear.

In the rotating spiral waves (RSW) regime, a base TVF structure is visible, but additional patterns appear due to axial non-axisymmetric elastic waves spiralling either upward or downward (Lacassagne *et al.* 2020) (figure 3 a, c, f). This results in additional and distinct ridges on the frequency maps (figure 3 b,g) that do not depend on Re, from the onset of which the critical Re for transition from/to RSW can be detected. The existence of TVF (that can be quite difficult to capture, see figure 3 a) thus spans from the appearance of spatial structures to the appearance of these ridges. They correspond to the temporal frequencies of RSW, i.e of the primary elastic instability, and their frequency scales as $f^k = k \times f_e$ with $f_e = 2c_e/\lambda$ the elastic frequency, $\lambda \simeq d$ a spatial wavelength, and $c_e = \sqrt{\mu/(\rho t_e)}$ the elastic wave celerity. The two first f^k frequencies are illustrated by horizontal dashed lines in figure 3 b and 3 g. Vertical dashed lines in figure 3 e for Re=133 denote the peaks corresponding to horizontal lines in figure 3 b. The related k values are reported in the figure caption.

Finally, in the elasto-inertial turbulence domain (EIT), the random alignment of flakes with a set of various spatial flow structures translates into an increasingly chaotic intensity signal and space-time plot (figure 3 a, d, f). The distinct peaks in the frequency maps that were present in RSW gradually merge into continuous spectra (figure 3 b, g, e). EIT thus consists in the appearance of spatial and temporal chaos on top of the organised TVF structure, through RSW and the multiplication of vortex merging and splitting events. Critical Re for RSW$\leftrightarrow$EIT transitions are identified from the frequency maps (figure 3b, g), when secondary RSW peaks can no longer be distinguished. Note that some of the spectral signature of RSW may persist into the EIT regime in the form of a consistent smoother peak (see figure 3 g), Re>170).

In RD experiments, an additional flow state is encountered in the form of upward spiralling vortices, and labelled SVF for Spiral Vortex flow (see figure 3 f). A summary

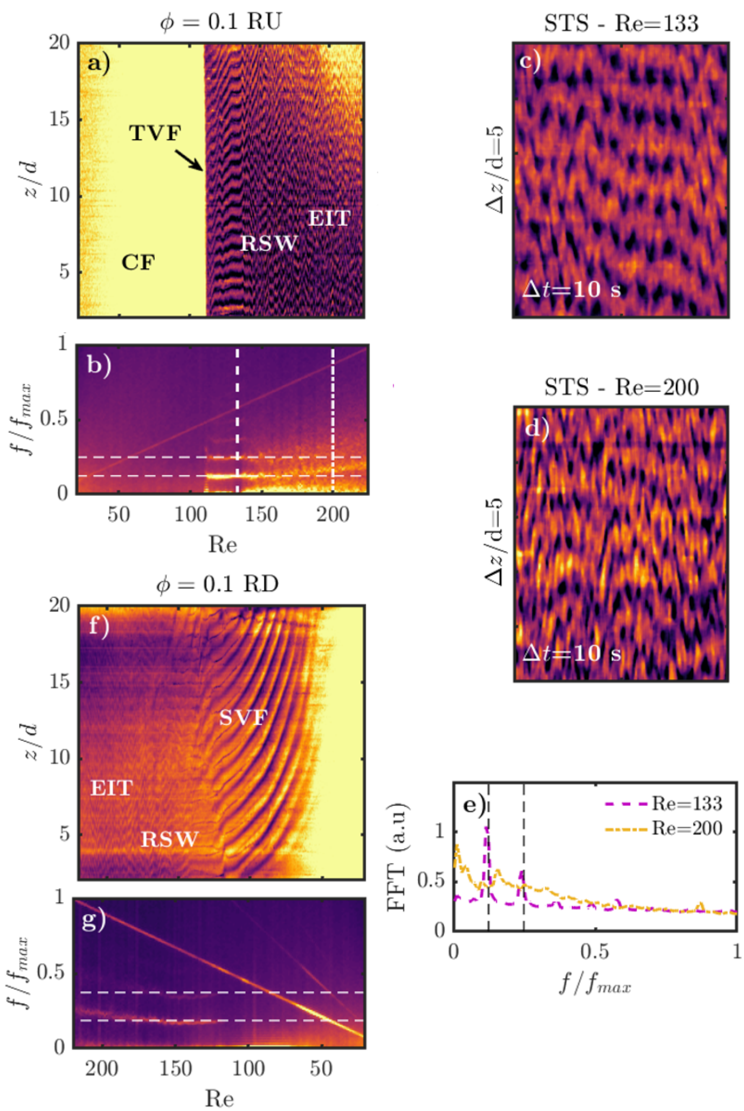

Figure 3: Example of ramp-up (RU, a,b), steady state (STS, c,d), and ramp-down experiments (RD,f,g) for a $\phi = 0.1$ fluid (false colors). a,f) are Re-space diagrams (flow maps), b,g) are frequency maps, c) and d) are space time diagrams at fixed Re, and e) shows temporal spectra extracted from the b) frequency map at Re corresponding to c) and d). Horizontal dashed lines in b) and g), and vertical dashed lines in e) denote elastic wave frequencies $f^k = k \times f_e$ with $k = [\frac{1}{3}, \frac{2}{3}]$ and $k = [\frac{1}{2}, 1]$ for the two first peaks in RU (b,e) and RD (g) respectively.

of critical Re for transitions is provided in figure 4 for RU and RD experiments (subfigures a and b, respectively). The experiments were repeated at least four times (see table 1) and excellent consistency on the succession of flow states was encountered. The reported visualisations correspond to single experimental runs, but critical Re values are

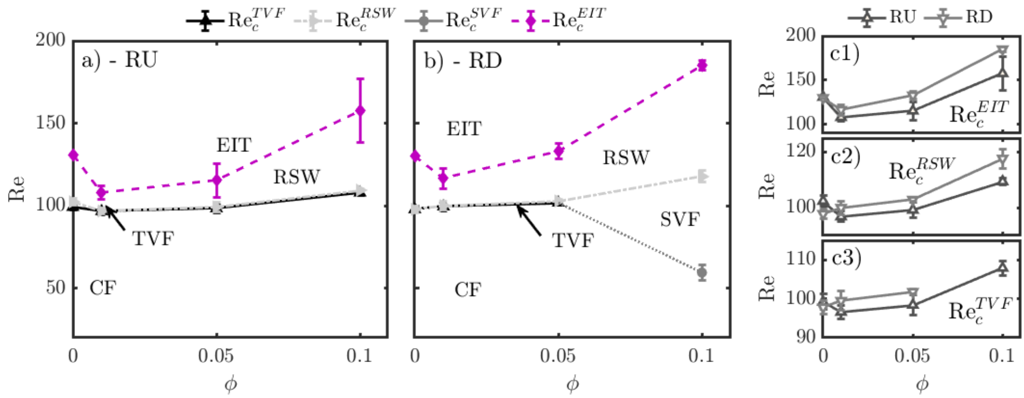

Figure 4: Critical Re-ϕ maps for transitions to TVF, RSW, EIT and SVF in RU (a) and RD (b) experiments. Hysteretic behaviours are illustrated for transitions to/from EIT, RSW and TVF in sub-figures c1, c2 and c3, respectively (triangles pointing upwards for RU, downwards for RD).

averaged over all repeats, and the standard deviations over critical Re provide error bars for figure 4.

It can be seen that the addition of particles initially decreases the critical Re for the CF$\longrightarrow$TVF transition at the lowest particle volume fraction, but as ϕ is increased above 0.01, the critical Re increases, stabilising the flow. The same trend is observed in figure 4 b) for the RD experiments for $\phi < 0.1$. Note that in Newtonian suspensions, the addition of particles in the same volume fraction range mostly leads to a minor destabilisation of the CF with respect to TVF (Majji *et al.* 2018; Ramesh *et al.* 2019; Gillissen & Wilson 2019). The opposite trend observed here must therefore be attributed to the combination of particles and viscoelastic fluid matrix; while both properties in isolation tend to destabilise CF compared to the Newtonian case, they have the opposite effect when combined.

For the $\phi = 0.1$ RD experiments, SVF is observed at Re values much lower than the critical Re for CF-TVF transition in RU. This new state is illustrated in the flow map and corresponding frequency map of figure 5. It appears to co-exist with RSW in the Re range from 120 to 140 (figure 5 a), close-up in 5 b)). We also note that SVF is not associated with any spectral signature on its own: the frequency map in the Re range of 20-120 is similar to that expected for TVF (figure 5 c)). Such spiralling behaviour was previously reported in particle suspensions in Newtonian fluids in RD (Majji *et al.* 2018) but also RU (Ramesh *et al.* 2019; Ramesh & Alam 2020), sometimes inter-penetrating or co-existing with other flow states (Majji *et al.* 2018; Ramesh & Alam 2020; Majji *et al.* 2018). The fact that the new state is found only in RD tests suggests a modification of the nature of primary instabilities in particle loaded Boger fluids at non-dilute volume fractions ($\phi \succeq 0.05$). SVF is unlikely to be caused by buoyancy or particle migration effects, since it arises when ramping down from chaotic states (EIT-RSW) in which particles are expected to be well mixed by strong axial flow velocity fluctuations. The co-existence of flow states, which was already observed for particles in Newtonian solvents (Ramesh *et al.* 2019; Ramesh & Alam 2020; Dash *et al.* 2020), is for the first time reported here for particle suspensions in Boger fluids.

The higher order transition to RSW (4 a and b) arises very soon after the onset of TVF (Lacassagne *et al.* 2020). After a slight destabilisation at $\phi = 0.01$, a stabilising

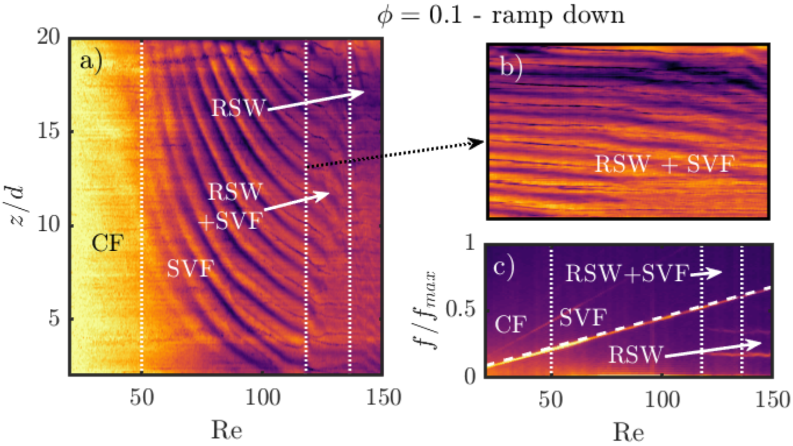

Figure 5: Illustration of the SVF state for RD experiments at $\phi = 0.1$, on the flow map (a) and frequency map (c) (focus from figure 3 f and g). Vertical dotted lines highlight transitions from RSW, RSW+SVF, SVF and CF from right to left (decreasing Re). A close-up of the frequency map in the coexisting state range RSW+SVF is provided in sub-figure b (Re axis ranging from 118 to 136, z/d axis from 5 to 20).

effect by particle addition is again reported, with critical Re values increasing with ϕ. RD results in figure 4 b) follow the same trend. Averaging on all experiments, TVF has a very narrow Re range of existence $\Delta \mathrm{Re}_{TVF} \sim 1$ with yet $\Delta t_{TVF} > 10 \times t_e$. It is the first in a series of transitions leading to more complex flow states. In some higher ϕ cases, TVF can sometimes not be seen clearly (figure 3 a) and the primary transition could be either CF↔TVF or CF↔RSW within the margin of error of this study. The results thus suggest that increasing particle concentration reduces $\Delta \mathrm{Re}_{TVF}$, promoting CF-RSW as the primary instability upon particle addition. However a precise understanding of this effect calls for a more accurate investigation in the Re=[100-120] range.

For the RSW to EIT transition, the trends for critical Re are globally similar to those previously reported for transition to RSW, i.e. a destabilisation by $\phi = 0.01$ followed by a stabilisation both in RU and RD cases, upon increased ϕ. This non-monotonic trend is more pronounced for the RSW↔EIT transition compared to those observed for lower order transitions. The combined effects of particles and viscoelasticity, which would have been expected to separately lead to earlier second order flow transitions, here again appear to delay transition to chaotic patterns.

3.2. *Effect of particle loading on RSW and EIT properties*

The effects of particle loading on EIT features can be characterised using spatio-temporal flow properties at a constant Reynolds number. Figure 6 shows two dimensional FFTs in time and space of STS experiments. Peaks of such spectra correspond to dominant time and length-scales of the flow. RSW is described by a set of discrete and identifiable peaks in space but also in time (see for example figure 6 c). On the other hand, EIT displays a broadband behaviour characteristic of a turbulent state, with no distinct peak (see e.g. figure 6 b). The temporal spectra projected on upper-right panels allow to distinguish between RSW (clear temporal peak, c) and EIT (no clear temporal peak, a,b,d). Figure 6 shows that the collapse of RSW spectra into broadband EIT, which occurs as Re is increased, is delayed by the increase in ϕ. In the $\phi = 0.01$ case (top line)

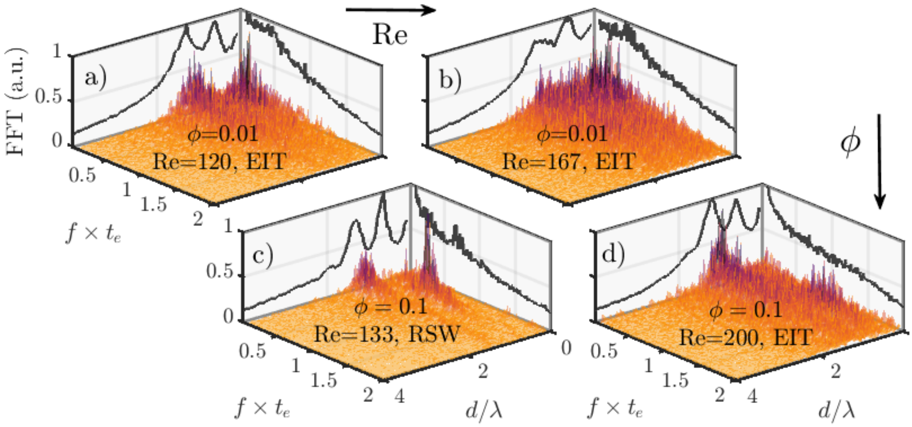

Figure 6: Two dimensional FFTs (time and space) of STS experiments for $\phi = 0.01$ (a,b) and $\phi = 0.1$ (c,d). Top left and top right panels on each sub-figure display mean spectra in the frequency and space dimensions, respectively. The spatial wavelength axis is scaled by the gap size d and the temporal frequency axis by $1/t_e$.

Re=167 (b) already corresponds to a turbulent signature without peaks, while for $\phi = 0.1$ (bottom line), peaks are still visible at Re=200 (d), although they are less distinct than at Re=133 (c). In other words, the presence of particles delays the transition to EIT, as previously observed, but also preserves the large scale spatial structure of RSW into EIT.

3.3. *Hysteretic behaviour*

At $\phi = 0$, critical Re for CF-TVF and TVF-RSW transitions are higher for RU experiments than for RD experiments (see figure 4 c2 and c3). This is the signature of a (moderately) sub-critical bifurcation (Martínez-Arias & Peixinho 2017). Particle addition reverses the hysteresis; even at the lower ϕ values, the critical Re values in RD experiments become larger than those found in RU tests, for both transitions. The flow transitions back to lower order states at higher Re that are seen in the RU tests, and the difference in critical Re values due to this reversed hysteretic behaviour increases with the order of the transition (larger for RSW-EIT transition than for CF-TVF transition), and with increasing ϕ.

The origin of such a reversed hysteretic behaviour may, at first, be attributed to elastic or inertial particle migration. Indeed, particles migrating away from the inner cylinder in CF during RU tests would induce lower inner viscosity and higher Re, leading to a lower apparent critical Re in ramp up compared to the ramp down case where particles are expected to be evenly dispersed and the viscosity homogeneous. This is in qualitative agreement with a similar reverse hysteresis observed by Ramesh *et al.* (2019) for the CF-TVF primary transition in Newtonian particle suspensions, suggesting that inertial migration may play a role. Moreover, the shortest time-scale at which elastic migration effects would arise, estimated according to the modelling of D'Avino *et al.* (2017), is found to be of about 50 s, comparable to and even shorter than the typical times particles spent in CF during a RU experimental protocol. Thus, elastic migration may also be at play when considering primary instabilities.

However, a stronger reversed hysteresis is observed for higher order RSW$\leftrightarrow$EIT transition, for which particles are expected to be well mixed in both states, which suggests that migration alone cannot explain the observed hysteretic phenomena. This new and striking result suggests that the particles act on elasto-inertial patterns with mechanisms other than migration, and more importantly that this action corresponds to a damping or attenuation of elasto-inertial features. Recent findings on local stress concentration and elastic thickening (see e.g. Yang & Shaqfeh (2018*a*,*b*)) in particles suspended in viscoelastic media might further explain this macroscopic behaviour.

4. Summary and conclusion

The results reported in this work show that particle addition to Boger fluids can significantly affect the elasto-inertial transitions and patterns in TC flow. Firstly, it tends to globally stabilise flow states with respect to the first and second order transitions, and delays the onset of elasto-inertial turbulence, thus stabilizing flows (after a small destabilisation in very dilute suspensions). Secondly, it modifies the spectral signature of EIT, by promoting energy concentration in large scale steeper peaks. Finally, it modifies the nature of flow transitions, with a reverse hysteresis behaviour and the occurrence of SVF in RD experiments.

All the previous observations underpin a damping of elastoinertial features by the presence of particles: a delay of their onset with increasing ϕ, a reduction of EIT chaotic features at constant Re for increased ϕ, and their reduction leading to a reverse hysteretic behaviour. An explanation for this could be that of an elastic thickening mechanism, that is to say an increase in viscosity associated with polymer-particle interactions. This phenomenon is due to the local elongation of polymer chains in inter-particle gaps, where strong shear or strain rates can be encountered; this leads in turn to strain hardening, a local increase in extensional viscosity (see for example Yang & Shaqfeh (2018*a*,*b*)) and a global increase in shear-viscosity.

Combining the presence of particles and viscoelasticity, which on their own would be expected to lead to flow destabilisation does not necessarily lead to stronger destabilisation. On the contrary, the destabilising effect of one complex fluid property may be cancelled out or reversed by the presence of another such property, as has recently been illustrated for the competition between shear-thinning and viscoelasticity (Lacassagne *et al.* 2021). Future work on this topic should in our opinion be focused on bridging the gap between local observation at the particle scale (Yang & Shaqfeh 2018*a*,*b*) and global flow characterisation in complex conditions and with non-negligible inertia. Further large scale experiments with various polymer chain extensional properties, together with the measurement of the shear-and strain rates in particle-free or particle loaded RSW and EIT flows, could bring further understanding on the role of extensional or elastic thickening. Practical considerations and industrial applications might also call for studies of particle suspensions at higher volume fractions, or higher blockage ratio (lower d_p/d ratio) for which particle particle interactions may become dominant (Royer *et al.* 2016).

Acknowledgements

Financial support for this work from the Engineering and Physical Sciences Research Council (EPSRC) Manufacturing the Future programme (No.EP/N024915/1) as well as the EPSRC DTP award EP/R513143/1 is gratefully acknowledged.

Declaration of interests

The authors report no conflict of interest.

REFERENCES

Baroudi, L., Majji, M. V. & Morris, J. F. 2020 Effect of inertial migration of particles on flow transitions of a suspension Taylor-Couette flow. *Physical Review Fluids* **5** (11), 114303.

Cagney, N., Lacassagne, T. & Balabani, S. 2020 Taylor–Couette flow of polymer solutions with shear-thinning and viscoelastic rheology. *Journal of Fluid Mechanics* **905**.

Dagois-Bohy, S., Hormozi, S., Guazzelli, E. & Pouliquen, O. 2015 Rheology of dense suspensions of non-colloidal spheres in yield-stress fluids. *Journal of Fluid Mechanics* **776**, R2.

Dash, A., Anantharaman, A. & Poelma, C. 2020 Particle-laden Taylor–Couette flows: higher-order transitions and evidence for azimuthally localized wavy vortices. *Journal of Fluid Mechanics* **903**.

D'Avino, G., Greco, F. & Maffettone, P. L. 2017 Particle Migration due to Viscoelasticity of the Suspending Liquid and Its Relevance in Microfluidic Devices. *Annual Review of Fluid Mechanics* **49** (1), 341–360.

Dherbécourt, D., Charton, S., Lamadie, F., Cazin, S. & Climent, E. 2016 Experimental study of enhanced mixing induced by particles in Taylor–Couette flows. *Chemical Engineering Research and Design* **108**, 109–117.

Dutcher, C. S. & Muller, S. J. 2009 Spatio-temporal mode dynamics and higher order transitions in high aspect ratio Newtonian Taylor–Couette flows. *Journal of Fluid Mechanics* **641**, 85–113.

Dutcher, C. S. & Muller, S. J. 2013 Effects of moderate elasticity on the stability of co- and counter-rotating Taylor–Couette flows. *Journal of Rheology* **57** (3), 791–812.

Fang, F., Aabith, S., Homer-Vanniasinkam, S. & Tiwari, M. K. 2017 9 - High-resolution 3D printing for healthcare underpinned by small-scale fluidics. In *3D Printing in Medicine* (ed. Deepak M. Kalaskar), pp. 167–206.

Fardin, M. A., Perge, C. & Taberlet, N. 2014 "The hydrogen atom of fluid dynamics" – introduction to the Taylor–Couette flow for soft matter scientists. *Soft Matter* **10** (20), 3523–3535.

Gillissen, J. J. J., Cagney, N., Lacassagne, T., Papadopoulou, A., Balabani, S. & Wilson, H. J. 2020 Taylor-Couette instability in disk suspensions: Experimental observation and theory. *Physical Review Fluids* **5** (8), 083302.

Gillissen, J. J. J. & Wilson, H. J. 2019 Taylor-Couette instability in sphere suspensions. *Physical Review Fluids* **4** (4), 043301.

Groisman, Alexander & Steinberg, Victor 1996 Couette-Taylor Flow in a Dilute Polymer Solution. *Physical Review Letters* **77** (8), 1480–1483.

Groisman, A. & Steinberg, V. 2004 Elastic turbulence in curvilinear flows of polymer solutions. *New Journal of Physics* **6**, 29–29.

Lacassagne, T., Cagney, N. & Balabani, S. 2021 Shear-thinning mediation of elasto-inertial taylor-couette flow. *Journal of Fluid Mechanics* **-**.

Lacassagne, T., Cagney, N., Gillissen, J. J. J. & Balabani, S. 2020 Vortex merging and splitting: A route to elastoinertial turbulence in Taylor-Couette flow. *Physical Review Fluids* **5** (11), 113303.

Liu, Z., Liu, L., Zhou, H., Wang, J. & Deng, L. 2015 Toothpaste microstructure and rheological behaviors including aging and partial rejuvenation. *Korea-Australia Rheology Journal* **27** (3), 207–212.

Majji, M. V., Banerjee, S. & Morris, J. F. 2018 Inertial flow transitions of a suspension in Taylor–Couette geometry. *Journal of Fluid Mechanics* **835**, 936–969.

Majji, M. V. & Morris, J. F. 2018 Inertial migration of particles in Taylor-Couette flows. *Physics of Fluids* **30** (3), 033303.

Martínez-Arias, B. & Peixinho, J. 2017 Torque in Taylor–Couette flow of viscoelastic polymer solutions. *Journal of Non-Newtonian Fluid Mechanics* **247**, 221–228.

Morris, J. F. 2020 Toward a fluid mechanics of suspensions. *Physical Review Fluids* **5** (11), 110519.

Ovarlez, G., Mahaut, F., Deboeuf, S., Lenoir, N., Hormozi, S. & Chateau, X. 2015 Flows of suspensions of particles in yield stress fluids. *Journal of Rheology* **59** (6), 1449–1486.

Ramesh, P. & Alam, M. 2020 Interpenetrating spiral vortices and other coexisting states in suspension Taylor-Couette flow. *Physical Review Fluids* **5** (4), 042301.

Ramesh, P., Bharadwaj, S. & Alam, M. 2019 Suspension Taylor–Couette flow: co-existence of stationary and travelling waves, and the characteristics of Taylor vortices and spirals. *Journal of Fluid Mechanics* **870**, 901–940.

Rida, Z., Cazin, S., Lamadie, F., Dherbécourt, D., Charton, S. & Climent, E. 2019 Experimental investigation of mixing efficiency in particle-laden Taylor–Couette flows. *Experiments in Fluids* **60** (4), 61.

Royer, J. R., Blair, D. L. & Hudson, S. D. 2016 Rheological Signature of Frictional Interactions in Shear Thickening Suspensions. *Physical Review Letters* **116** (18), 188301.

Saint-Michel, B., Bodiguel, H., Meeker, S. & Manneville, S. 2017 Simultaneous Concentration and Velocity Maps in Particle Suspensions under Shear from Rheo-Ultrasonic Imaging. *Physical Review Applied* **8** (1), 014023.

Saint-Michel, B., Manneville, S., Meeker, S., Ovarlez, G. & Bodiguel, H. 2019 X-ray radiography of viscous resuspension. *Physics of Fluids* **31** (10), 103301.

Schaefer, C., Morozov, A. & Wagner, C. 2018 Geometric scaling of elastic instabilities in the Taylor-Couette geometry: A theoretical, experimental and numerical study. *Journal of Non-Newtonian Fluid Mechanics* **259**, 78–90.

Yang, M. & Shaqfeh, E. S. G. 2018*a* Mechanism of shear thickening in suspensions of rigid spheres in Boger fluids. Part I: Dilute suspensions. *Journal of Rheology* **62** (6), 1363–1377.

Yang, M. & Shaqfeh, E. S. G. 2018*b* Mechanism of shear thickening in suspensions of rigid spheres in Boger fluids. Part II: Suspensions at finite concentration. *Journal of Rheology* **62** (6), 1379–1396.